EES Batteries

PAPER

View Article Online
View Journal | View Issue

Cite this: *EES Batteries*, 2026, **2**, 282

Influence of the backbone chemistry and side-chain spacer flexibility in sodium single-ion conducting polymer electrolyte for sodium-batteries

Clemens Wunder,[a,b] Laura Hildebrand,[a,b] Leo Gräber,[a,b] Alberto Varzi,[a,b] Dominic Bresser,[a,b] Maider Zarrabeitia *[a,b] and Stefano Passerini *[a,b,c]

Single-ion conducting polymer electrolytes (SIPEs) have garnered increasing attention in recent years due to their wide electrochemical stability window (ESW), excellent thermal stability, and superior electrochemical performance when impregnated with a molecular transporter. This work investigates the influence of the flexibility of the sulfonyl(trifluoromethanesulfonyl) imide anionic center on 3D crosslinked SIPEs composed of a sodium salt monomer (SSM), either sodium 4-styrenesulfonyl (trifluoromethanesulfonyl)imide, sodium sulfonyl (trifluoromethanesulfonyl)imide methacrylate (NaMTFSI) or sodium ((1,1,2,2-tetrafluoro-2-(1,1,2,2-tetrafluoro-2-iodoethoxy)ethyl)sulfonyl)-(trifluoro-methanesulfonyl)imide, bound to the pentaerythritol tetrakis(3-mercaptopropionate) (PETMP) and pentaerythritol tetraacrylate (PET4A), also including poly(vinylidene fluoride-*co*-hexafluoropropylene) to enhance the mechanical properties. Sodium metal-based cells employing Prussian White (PW) as cathode deliver the highest specific capacity and capacity retention by using NaMTFSI as SSM due to its increased flexibility and chemical stability. Additionally, the impact of the polymer backbone chemistry on the porosity, mechanical, thermal, and electrochemical properties has been investigated using either PET4A, hexa-1,5-diene (diene), 1,3,5-triallyl-1,3,5-triazine-2,4,6(1*H*,3*H*,5*H*)-trione, or dipentaerythritol hexaacrylate, together with PETMP and NaMTFSI. The results reveal that the diene-based-SIPE leads to a higher pore structure, exhibiting a high ionic conductivity of 1.2×10^{-4} S cm^{-1} at RT, thermal stability up to 270 °C, wide ESW (4.2 V vs. Na$^+$/Na), and the Na|SIPE|PW cells delivering 119 mAh g^{-1} after 200 cycles with excellent Coulombic efficiency.

Received 7th August 2025,
Accepted 25th November 2025

DOI: 10.1039/d5eb00145e

rsc.li/EESBatteries

Broader context

The global energy transition is driving an urgent need for sustainable batteries with high energy density, but lower costs. Among the several next-generation battery candidates, sodium batteries are the best option due to their comparable performance to $LiFePO_4$-based lithium-ion batteries (LIBs), possibly at a lower cost. Nonetheless, present sodium batteries employ liquid electrolytes offering high ionic conductivity, but carrying safety hazards due to their high volatility and flammability, as well as to uneven Na deposition. Therefore, safer electrolytes are desired, such as single-ion polymer electrolytes (SIPEs), which promise to address both challenges lowering the flammability and mitigating dendrite growth through high sodium-ion transference numbers. This approach provides a new paradigm for the design of high-performance SIPEs and represents a significant step toward the realization of safe, high-energy-density Na-metal batteries (NMBs).

Introduction

Lithium-ion batteries (LIBs) dominate the market of portable electronic devices and, more recently, the electric vehicle (EV) market due to their high energy densities and long cycle life.[1] However, the fluctuating cost and limited availability of LIB resources, such as lithium, natural graphite, nickel, and cobalt, among others, could hamper their use mainly in large-scale stationary energy storage applications.[2] Therefore, alternative batteries, which do not exhibit material resource issues, are the best candidates to complement LIBs.[3,4]

Among several candidates, sodium-ion batteries (SIBs) are the best option due to their comparable performance to $LiFePO_4$-based LIBs, possibly at a lower cost,[5] becoming an excellent solution for energy storage devices in large-scale grid applications.[6–9] SIBs are based on liquid electrolytes offering high ionic conduc-

[a]*Helmholtz Institute Ulm (HIU), Helmholtzstr. 11, 89081 Ulm, Germany. E-mail: maider.ipina@kit.edu, stefano.passerini@kit.edu*
[b]*Karlsruhe Institute of Technology (KIT), P.O. Box 3640, 76021 Karlsruhe, Germany*
[c]*Austrian Institute of Technology (AIT), Center for Transport Technologies, Giefinggasse 2, 1210 Wien, Austria*

tivity at room temperature (RT). However, this results in safety hazards due to their high volatility and flammability.[10] Therefore, safer electrolytes are desired, such as solid-state electrolytes (SSEs). Among SSEs, organic polymer electrolytes are of special interest due to their high flexibility, self-standing properties, modularity, interfacial properties and thermal stability.[11–13] Nevertheless, neat solid polymer electrolytes (SPEs), also known as dry polymer electrolytes, suffer from low ionic conductivity at RT and high interfacial resistances.[14,15] The incorporation of carbonates or ionic liquids to form quasi-solid-state polymer electrolytes could enhance the ionic conductivity and reduce the interfacial resistance.[4,16] However, the incorporation of a conducting salt together with carbonates bears the risk of dendrite growth upon cycling due to the build-up of a concentration gradient, which becomes even more severe when cycling at high rates and/or upon prolonged periods.[17] In this scenario, the most favorable strategy reported until now to avoid dendrite growth is the development of single-ion conducting polymer electrolytes (SIPEs), where the anion diffusion across the electrolytes is hindered due to the anion being chemically bonded to the polymer backbone, while only the cation can move freely.

SIPEs frequently contain the (trifluoromethanesulfonyl)(sulfonyl)imide ($-SO_2-N^--SO_2-CF_3$) anion bound to the polymer chain, because of the negative charge being well delocalized in the anion owing to the neighboring electron-withdrawing $-SO_2-$ and $-CF_3$ groups. Examples include poly(sodium1-[3-(methacryloyloxy)propylsulfonyl]-1-(trifluoromethanesulfonyl) imide) (PNaMTFSI),[18] sodium multi-block ionomers,[19] or, as very recently reported by us, a sodium 4-styrenesulfonyl (trifluoromethanesulfonyl)imide (NaSTFSI)-based SIPE.[20] However, the anionic center is not the only parameter that should be considered when designing SIPEs. For example, the chemistry, size and flexibility of the spacer arm may also affect the SIPE's physicochemical and electrochemical properties.[21] In addition, the cross-linking sites of the backbone components may contribute to the formation of different 3D networks and, in turn, hinder or facilitate the cation diffusion, thus affecting the ionic conductivity and, as a result, the electrochemical performance. To the best of our knowledge, though, no studies have been conducted on the influence of the side-chain spacer arm chemistry and the cross-linking degree of the 3D network monomers for Na-based SIPEs.

Accordingly, in this work, we have investigated the mechanical, thermal and electrochemical properties of various SIPEs *versus* the strength and composition of the backbone and the degree of cross-linking. The results reveal that the physicochemical and electrochemical properties of the SIPE depend on the backbone composition, the amount and size of pores and the flexibility of each anionic center.

Experimental section

Synthesis of NaSTFSI, NaMTFSI and NaFTFSI sodium salt monomers

NaSTFSI was synthesized as recently reported,[22] sodium sulfonyl (trifluoromethanesulfonyl)imide methacrylate (NaMTFSI) was purchased from Specific Polymer, and sodium ((1,1,2,2-tetrafluoro-2-(1,1,2,2-tetrafluoro-2-iodoethoxy)ethyl)sulfonyl)-(trifluoro-methanesulfonyl)imide (NaFTFSI) was synthesized following an earlier described procedure (see Fig. S1 for the structure of the three sodium salt monomers (SSMs)).[23,24] The structural and chemical confirmation for the successful synthesis of NaSTFI, previously reported,[20] and NaFTFSI is displayed in Fig. S2 and Fig. S3.

Membrane fabrication

The SIPE membrane was fabricated *via* solvent casting. First, the investigated backbone components, such as hexa-1,5-diene (diene, Thermo Scientific, 98%), 1,3,5-triallyl-1,3,5-triazine-2,4,6(1*H*,3*H*,5*H*)-trione (trione, Merck, >96%), pentaerythritol tetraacrylate (PET4A, VWR Merck, 99%) or dipentaerythritol hexaacrylate (PET6A, BLD Pharmatech, 95%), were dissolved with pentaerythritol tetrakis(3-mercaptopropionate) (PETMP, Merck, 97%) and poly(vinylidene fluoride-*co*-hexafluoropropylene) (PVDF-HFP, Merck – pellet) in DMF (7 mL, VWR chemicals 99.8%). Meanwhile, the SSM, *i.e.*, NaSTFSI (in-house-made), NaMTFSI (Specific Polymers) or NaFTFSI (in-house-made), was dissolved in DMSO (1 mL, VWR chemicals, >99%). The solutions were stirred separately for 3 hours and then mixed for an additional 2 hours. The combined solutions were cast into Teflon disks (∅ = 62 mm) covered with perforated Al foil, and heated for 28 hours at 80 °C, resulting in self-standing SIPE membranes with a thickness of approximately 120 μm (±40 μm). The SIPE membranes were cut into 16 mm discs, dried at 70 °C under vacuum for 3 hours, and then transferred into a glovebox (O_2 and H_2O levels <0.1 ppm). The molecular transporter mixture, consisting of ethylene carbonate (EC, Aldrich, 99%), dimethyl carbonate (DMC, Aldrich, 99.9%) and fluoroethylene carbonate (FEC, Aldrich, 99%), in a volume ratio of 49 : 49 : 2 (2 mL), was incorporated into the SIPEs at 60 °C for 48 hours prior to use as electrolyte. This specific mixture was chosen due to its similarities with alkali-ion batteries, where an EC:DMC mixture is typically used as a solvent. In addition, a small amount of FEC was incorporated due to its ability to form a stable NaF-rich SEI on the Na metal electrode, enhancing the performance in Na metal cells. The average solvent uptake of the SIPEs was 50 wt.% (±5 wt.%). The SIPEs based on different SSMs are referred to as NaSTFSI-SIPE, NaMTFSI-SIPE and NaFTFSI-SIPE, while the SIPEs with different polymer backbone components are labelled as follows: diene-, trione-, PET4A- and PET6A-SIPE.

Physicochemical and thermal characterization

The structure of the NaFTFSI SSMs was investigated using liquid nuclear magnetic resonance (^{19}F-NMR), which was measured on a Bruker Avance 400 (^{1}H at 400 MHz) spectrometer using DMSO-D_6 as the solvent. The NaSTFSI structure was previously confirmed.[20] The thermal properties and thermal phase transitions of the SIPEs were assessed with thermogravimetric analysis (TGA – Netzsch TG 209 F1) and differential scanning calorimetry (DSC – Discovery series, TA Instrument). TGA was performed by sealing the dry SIPE mem-

branes (~5 mg) in Al crucibles and heating them at 5 °C min^{-1} to 600 °C under N_2. Three DSC sweeps were measured between −100 °C and 200 °C using a heating rate of 5 °C min^{-1} under N_2 (gas flow: 10 ml min^{-1}).

Mechanical and structural characterization

The mechanical properties were studied by elongating the dry SIPE until failure and recording a stress–strain curve. The ~100 μm thick dry SIPE membranes were cut into dumbbell specimens using the cutting press ZwickRoell ZCP 020. The tensile tests were performed on a universal testing machine, Inspect Table from Hegewald and Peschke (Nossen, Germany), equipped with a 1.5 kN force transducer. The tests were performed at RT with a testing speed of 5 mm min^{-1}.

Small-angle X-ray scattering (SAXS) patterns were collected using a Xeuss 3.0c (Xenocs – Grenoble, France) equipped with an Eiger2 1 M detector. The sample-to-detector distance was set to 1100 mm, resulting in an overall usable Q-range of 0.00014 to 0.247 $Å^{-1}$. A Cu Kα source was used, with a beam size of 0.35 × 0.35 mm^2, resulting in a flux of ~10^7 photons per second. The samples were stuck to a perforated metal plate using standard Scotch Tape®. The polyvinylidene fluoride (PVDF) powder measurements were performed by applying it to the adhesive tape, completely covering the holes of the plate. Instead, the dry SIPE membranes were adhered to the holder in a manner that only the membrane covered the hole. The sample chamber of the instrument was kept under vacuum (p = 8 × 10^{-5} bar) during the experiment. Each measurement was performed for 10 minutes to ensure a good signal-to-noise ratio. The collected 2D scattering patterns were azimuthally integrated over the entire circumference to obtain the scattering curves as a function of q. The intensity was scaled to absolute units using the sample transmission and the calibration with a glassy carbon secondary standard. When needed, the plain scotch tape background was also collected and subtracted from the total scattering curve. Data treatment was performed with the Xsact software from Xenocs.

The porosity was examined by gas adsorption/Brunauer–Emmett–Teller (BET) in combination with DFT analysis in an Autosorb-iQ-MP/XR analyzer (Quantachrome) by Ar adsorption at 87 K. The temperature was controlled using a cryoTune 87 from 3P instruments. Each sample was degassed at 150 °C for 20 hours prior to measurement. A zeolite/silica (spherical & cylindrical) pore system was assumed for the non-local DFT equation to determine the pore size distribution.

Electrochemical characterization

The ionic conductivity of the SIPEs, including 50 wt.% of molecular transporters (EC:DMC:FEC, 49:49:2 in vol.%), was determined in coin cell configuration with Al disk electrodes. The measurements were performed by electrochemical impedance spectroscopy (EIS – Solartron SI 1260/1287 Impedance Analyzer) in the frequency range from 1 Hz to 1 MHz, with an amplitude of 10 mV at various temperatures, ranging from 10 to 90 °C using a climatic chamber (Binder KB23). After setting the desired temperature, the coin cells were allowed to rest for 3 hours to reach equilibrium. The impedance spectra were fitted by using RelaxIS 3 software with an RPfit, to calculate the ionic conductivity (σ), considering the thickness (d) and the area (A) of the SIPE membranes and the determined interfacial resistance (R) from the Nyquist plot.

The stripping/plating tests were performed by assembling symmetric Na|SIPE|Na coin cells (using 12 mm Na discs produced by rolling out and cutting Na foil, Acros Organic) and applying a current density between 10 and 50 μA cm^{-2}. Each cell was cycled for 5 cycles at each current (1 hour for each cycle), before the current was increased by 10 μA cm^{-2}. Afterwards, each cell was cycled at 50 μA cm^{-2} for additional 25 cycles. Potentiostatic EIS (PEIS) measurements were collected after the first and last cycles at each current density, after the first and the last cycles of the long-term cycling step performed at 50 μA cm^{-2}.

The electrochemical stability voltage window of SIPEs was assessed using linear sweep voltammetry (LSV) of cells employing Al and Na metal discs as the working and counter electrodes, respectively. The coin cells were left in rest for 6 hours and then subjected to a voltage scan (30 μV s^{-1}) from OCV up to 7.0 V or down to −2.0 V vs. Na^+/Na, using fresh cells for each scan. The stripping/plating and LVS tests were performed at 40 °C (Binder climatic chamber KB23) using the Biologic SAS VMP-3e potentiostat.

Galvanostatic cycling tests of the full coin cells (CR2032, S4R) were conducted at 40 °C using Prussian White ($Na_2Fe[Fe(CN)_6]$, PW, Altris) as the cathode and Na metal as the anode, using a Maccor 4000 battery tester. The cycling protocol was as follows: initial cycle at C/50 rate (1C = 150 mAh g^{-1}), followed by 5 cycles at C/20 rate and ongoing cycles at C/10 rate until failure. The PW electrodes consisted of 80 wt.% PW, 10 wt.% C45 (Imerys), 5 wt.% sodium carboxymethyl cellulose (Na-CMC, Sigma-Aldrich) and 5 wt.% styrene–butadiene rubber (SBR, ZEON) with an average mass loading of 1.3 ± 0.4 mg cm^{-2}. These electrodes were dried at 140 °C and 10^{-7} mbar for 24 hours prior storage in glovebox (O_2 < 0.1 ppm, H_2O < 0.1 ppm).

Results and discussion

Influence of the sodium salt monomer side-chain spacer

The chemistry and properties (such as flexibility) of the side-chain spacer, connecting the $–SO_2–N–SO_2–CF_3$ anion to the polymer backbone, are crucial for the ionic conductivity of SIPEs. For example, the chemical composition of the side-chain spacer influences the charge delocalization of the cationic charge carrier, and in turn, the ionic conductivity, as well as it may also contribute to the solid electrolyte interphase (SEI) formation. Therefore, the influence of the side-chain spacer was investigated using a PET4A, PETMP and PVDF-HFP SIPE with either NaSTFSI (which has a sterically demanding and rigid benzene ring with -TFSI-based anion center to delocalize the electron, analogues to the reported one for Li-batteries), NaMTFSI (which has a flexible and long side-chain spacer that can facilitate the Na^+ transport), or NaFTFSI (which

also has a flexible, but fluorinated side-chain spacer and hence, even higher electron delocalization than the NaSTFSI) SSM (Fig. 1a).

The thermal stability of all three dry SIPEs was assessed using TGA (Fig. 1b) between 30 °C and 600 °C. The degradation temperature was determined by the onset of rapid mass loss, represented by the dotted lines, which was evaluated by drawing a line that starts at the beginning and extends along the next measurement points (tangent method). The start of the decomposition temperature was selected as the first temperature at which the line did not fit the experimental data. The TGA curves indicate that the NaSTFSI- and NaFTFSI-SIPE membranes showed thermal stability up to 300 °C, while the NaMTFSI-SIPE showed a slightly lower thermal stability up to 270 °C. This poorer stability is due to the ester (R–(C═O)–O–R, R = alkyl group) group that exhibits easier bond breaking upon heating compared to the benzene ring or the fluorinated alkyl chain (–CF_2–CF_2–O–CF_2–CF_2–).[20,24,25] The NaFTFSI-SIPE exhibited an additional shoulder at around 450 °C, indicating that NaFTFSI's decomposition occurs at two distinct temperatures. The feature at 300 °C corresponds to the decomposition of the backbone, while that at 450 °C arises from the decomposition of the side chain. This indicates that the NaFTFSI SSM is even more thermally stable than the other two studied SSMs.

The phase transitions of the dried SIPEs were investigated using DSC (Fig. 1c) within the −20 °C to 200 °C temperature range and a rate of 5 °C min^{-1}. All SIPEs showed a glass transition temperature (T_g) at about 30 °C and an exothermic crystallization temperature (T_c) around 100 °C, matching the crystallization temperature of PVDF-HFP.[26]

The SIPEs were soaked in EC:DMC:FEC (49:49:2 vol.%) solution, serving as a molecular transporter, at 60 °C for 48 hours

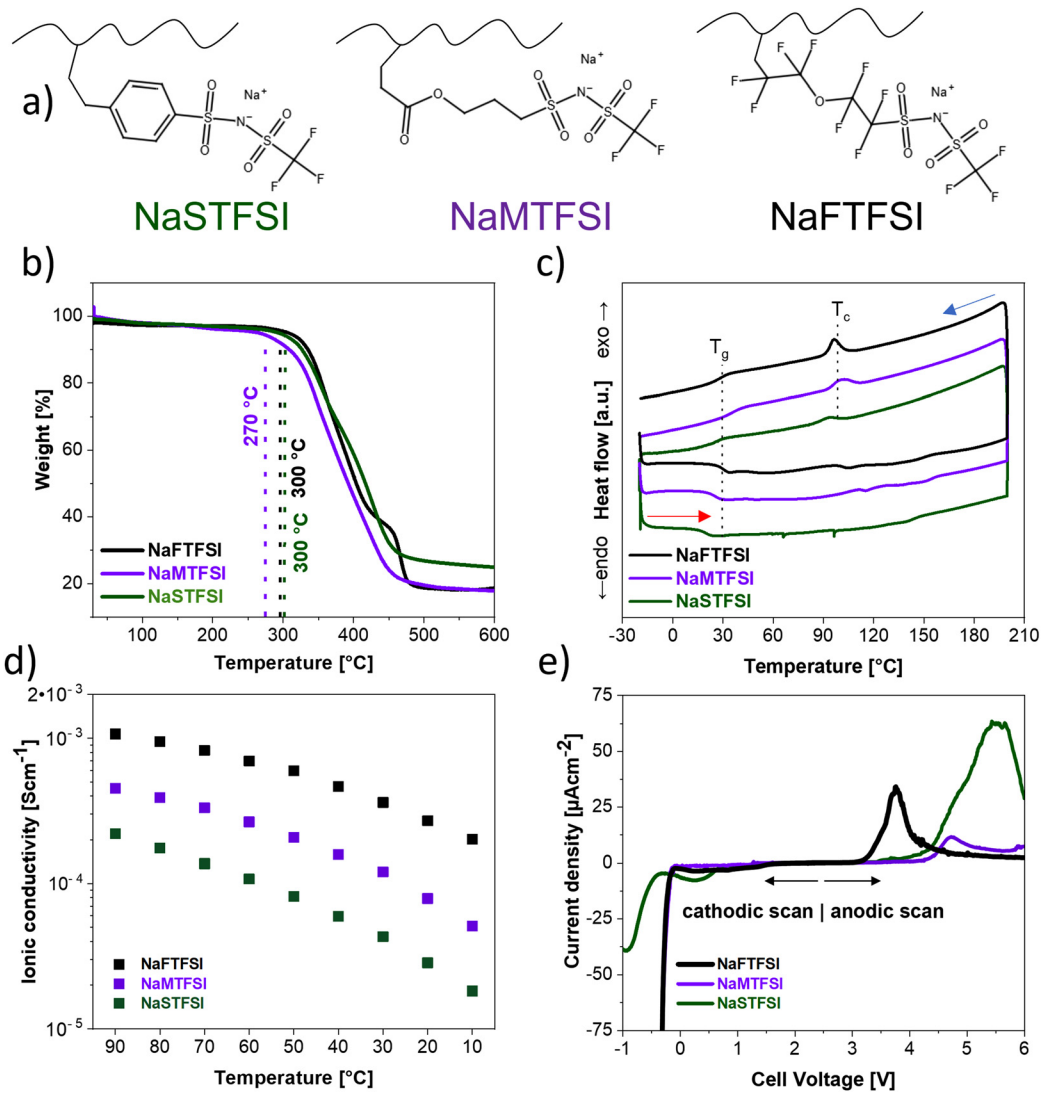

Fig. 1 (a) Chemical structure of the studied SSMs. (b) TGA and (c) DSC (heating rate of 5 °C min^{-1}, N_2 atmosphere for both experiments) data of NaSTFSI- (green), NaMTFSI- (purple) and NaFTFSI (black)-dry SIPEs. (d) Temperature-dependent ionic conductivity and (e) electrochemical stability window (Na||SIPE||Al, scan rate of 30 μV s^{-1} at 40 °C) of NaSTFSI-, NaMTFSI- and NaFTFSI-based SIPEs containing 50 wt.% of EC:DMC:FEC.

prior to the ionic conductivity measurements. The uptake was determined to be 50 wt.% of the final electrolyte membrane by differential weighing. The ionic conductivity measurements were performed between 10 °C and 90 °C (Fig. 1d), starting from 20 °C and step-wise reaching 90 °C (increasing 10 °C per step) followed by a stepwise cooling to 10 °C. The ionic conductivity variation with temperature exhibits the Vogel–Tamman–Fulcher (VTF, see Fig. S4 for comparison with $\ln(\sigma)$ *vs.* $1000/T$ plot) behaviour typically observed in SIPEs and other electrolyte systems.[27,28] At 20 °C, NaSTFSI-SIPE delivered the lowest ionic conductivity of 2.8×10^{-5} S cm^{-1} (2.2×10^{-4} S cm^{-1} at 90 °C), followed by NaMTFSI-SIPE, which reached 7.9×10^{-5} S cm^{-1} (4.5×10^{-4} S cm^{-1} at 90 °C), and NaFTFSI-SIPE reaching 2.7×10^{-4} S cm^{-1} (1.1×10^{-3} S cm^{-1} at 90 °C). The lowest ionic conductivity of NaSTFSI-SIPE resulted from the shorter and rigid benzene side-chain spacer, hindering the movement of the anionic center. Meanwhile, NaMTFSI-SIPE has a similar chain length but a more flexible arm, which facilitates Na^+ conduction. The ionic conductivity was even higher for the fluorinated NaFTFSI-SIPE due to the slightly longer chain and the presence of fluorine atoms, which withdraw and delocalize the negative charge across the whole SSM rather than just in the anionic center.

The electrochemical stability window (ESW) was investigated by LSV (Fig. 1e). The NaMTFSI- and NaSTFSI-SIPE exhibited a good electrochemical stability from 0 V (*i.e.*, prior Na plating) up to 4.2 V vs. Na^+/Na (threshold for the voltage onset was 25 μA cm^{-2}). In comparison, the NaFTFSI-SIPE exhibited lower oxidation stability, as indicated by the peak at around 3.5 V. The lower value of the oxidation threshold voltage may be related to the oxidation of the fluorine-rich side chain and side reactions, resulting in the formation of a passivation layer.[19] Indeed, such a low oxidation stability suggested NaFTFSI-SIPE not to be an appropriate SIPE for PW cathode-based Na metal cells, since the end-of-charge voltage of PW is around 4.0 V vs. Na^+/Na . Regarding cathodic stability, NaMTFSI- and NaFTSI-SIPEs exhibited a more rapid current increase below 0 V compared to NaSTFSI-SIPE, indicating lower polarization and good compatibility with Na metal due to the rapid Na deposition. Summarizing the anodic and cathodic scan results,

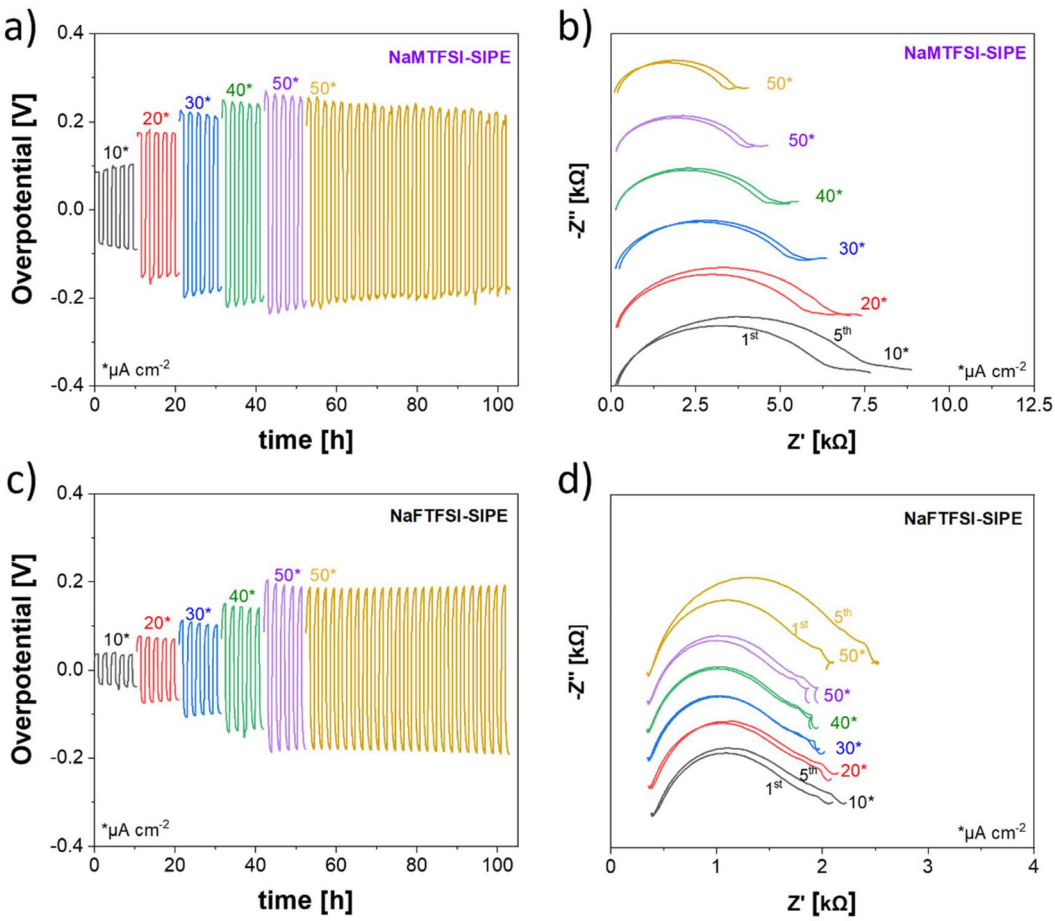

Fig. 2 Na stripping/plating tests at different current densities (from 10 to 50 μA cm^{-2}) at 40 °C and the corresponding Nyquist plot (after the first and 5th cycle at each current density: 10 μA cm^{-2} – black, 20 μA cm^{-2} – red, 30 μA cm^{-2} – blue, 40 μA cm^{-2} – green and 50 μA cm^{-2} – purple, as well as after 1st and 5th in the long-term cycling at 50 μA cm^{-2} – yellow) of (a and b) NaMTFSI-, and (c and d) NaFTFSI-SIPEs, respectively with 50 wt. % of EC:DMC:FEC (49:49:2 vol.%) molecular transporter.

NaMTFSI-SIPE appears to be the most appropriate electrolyte for application in full-cells. However, to further investigate the plating/stripping behavior of SIPEs, additional symmetric cells (Na||SIPE||Na) were tested with current densities between 10 and 50 μA cm^{-2} (Fig. 2 and Fig. S5). The interfacial resistance evolution upon cycling was studied using EIS, which showed an increase during long-term cycling, reaching up to 15 kΩ for the NaSTFSI-SIPE (Fig. S5b). In contrast, the NaMTFSI-SIPE (Fig. 2b) showed a slight decrease upon cycling, reaching 3.5 kΩ at 50 μA cm^{-2}, while the interfacial resistance of NaFTFSI-SIPE (Fig. 2d) remained rather constant at around 2.5 kΩ. The small increase might be related to the fact that the $-CF_2$ groups may undergo dehydrofluorination, yielding the formation of a NaF-rich SEI, as observed with NaSTFSI-SIPE,[20] but resulting into a loss of the initial properties, such as ionic conductivity, thereby increasing the interfacial resistance. Nevertheless, these results are in line with the observed overpotential values. The low and rather stable interfacial resistances of NaMTFSI- and NaFTFSI-SIPE suggest that they contribute to the formation of a good ion-conducting SEI, rendering both SIPEs suitable for Na metal cells.

The electrochemical performance in quasi-solid-state Na|SIPE|PW cells was also investigated. The cells employing NaSTFSI- (Fig. 3a) and NaFTFSI-SIPEs (Fig. 3b) exhibited high polarization. Meanwhile, the NaMTFSI-SIPE based-cell (Fig. 3c) showed lower polarization, clearly displaying the two characteristic plateaus of PW at 3.0 and 3.3 V, in line with the lower polarization visible during stripping/plating.[20] The PW cathode tested with NaSTFSI-SIPE delivered an initial charge and discharge capacity of 144 and 141 mAh g^{-1}, respectively. Meanwhile, the cells composed of NaFTFSI- and NaMTFSI-SIPE exhibited 172/148 mAh g^{-1} and 155/142 mAh g^{-1}, respectively. The high irreversibility of PW in NaFTFSI-SIPE is likely related to SIPE oxidation, as indicated by LSV and confirmed by the charge capacity being greater than the theoretical value.

The long-term stability of the cells was also investigated (Fig. 3d). The Na|NaMTFSI-SIPE|PW cell delivered the highest capacity and exhibited the best cycling stability, in agreement with the higher stability against Na observed in the stripping/plating tests and the excellent oxidation stability observed *via* LSV. Indeed, the Na|NaMTFSI-SIPE|PW cell showed a capacity

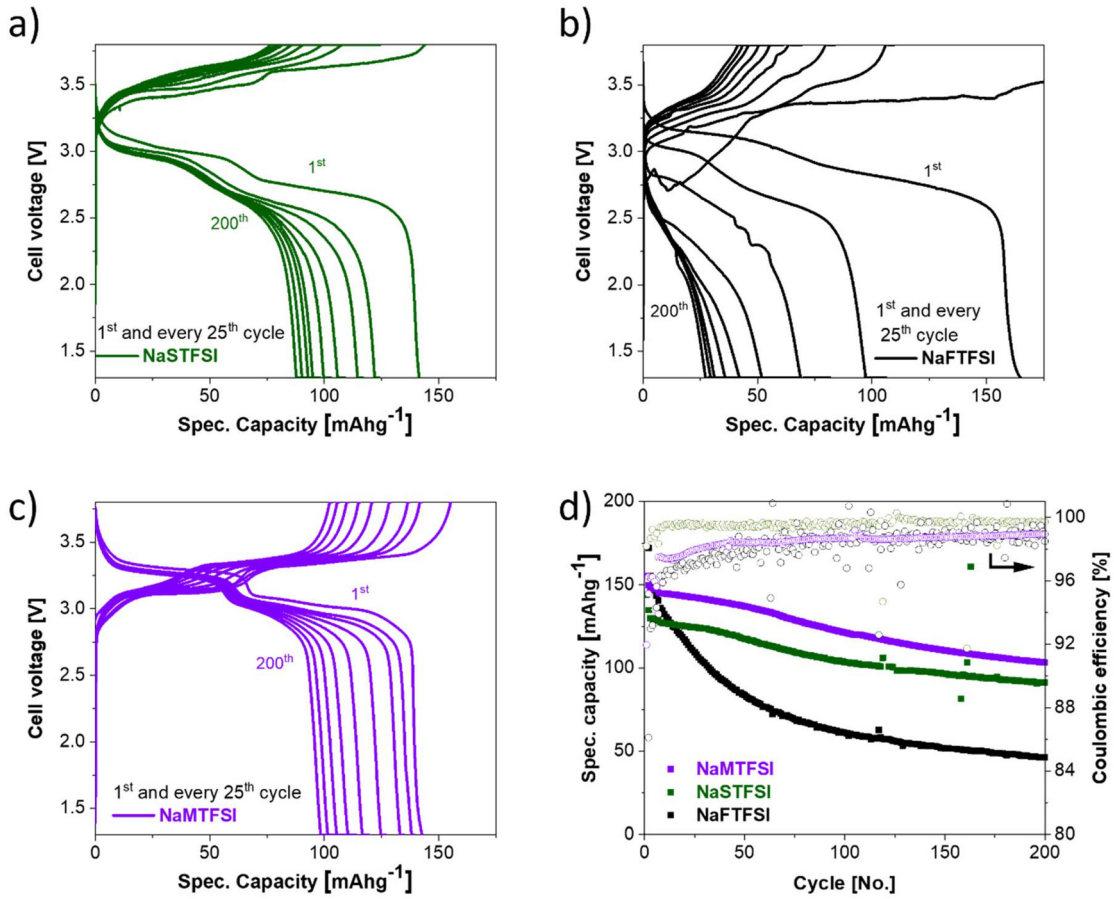

Fig. 3 Voltage profile of Na||PW cells using (a) NaSTFSI-, (b) NaFTFSI- or (c) NaMTFSI-SIPEs, and the corresponding (d) specific capacity and Coulombic efficiency. In all SIPEs, EC:DMC:FEC (49:49:2 vol.%) is incorporated, serving as molecular transporter. The galvanostatic cycling tests are conducted at a C-rate of C/50 in the first cycle, followed by 5 cycles at C/20, and continuous cycling at C/10 between 3.8 V and 1.3 V at 40 °C.

retention of 72%, followed by Na|NaSTFSI-SIPE|PW (70%) and Na|NaFTFSI-SIPE|PW (31%) cells after 200 cycles.

With regard to Coulombic efficiency, the NaFTFSI-SIPE-based PW cell delivered low and fluctuating values, due to the SIPE decomposition reactions described above. However, the Coulombic efficiency of the cell based on NaSTFSI-SIPE went above 99% after a few cycles (ICE = 98%). On the other hand, the NaMTFSI-SIPE-based cells delivered initially low Coulombic efficiency (<97%), suggesting the occurrence of decomposition reaction(s). This may be attributed to the ester splitting reaction of the methacrylate side chain spacer, induced by the high proton content, together with a high fluorine content near the Na metal anode (Fig. S6).

While the continuous capacity decay of these quasi-solid-state Na cells highlights the need for further optimization, the electrochemical performance obtained with NaMTFSI- and NaSTFSI-SIPEs indicated a promising direction for designing SIPEs for solid-state Na-metal batteries.

Influence of the backbone components

The backbone structure and chemistry of the polymer membrane are expected to influence the thermal, mechanical and electrochemical properties of the SIPEs as well. Thus, the influence of the backbone was investigated using the most promising SSM, NaMTFSI, with PETMP (Fig. 4a, blue) and either diene, trione, PET4A, or PET6A as backbone components, which were blended with PVDF-HFP and incorporated with 50 wt.% of the molecular transporter mixture. The membranes are labeled by the varying backbone components as diene-, trione-, PET4A- and PET6A-SIPE, respectively (see

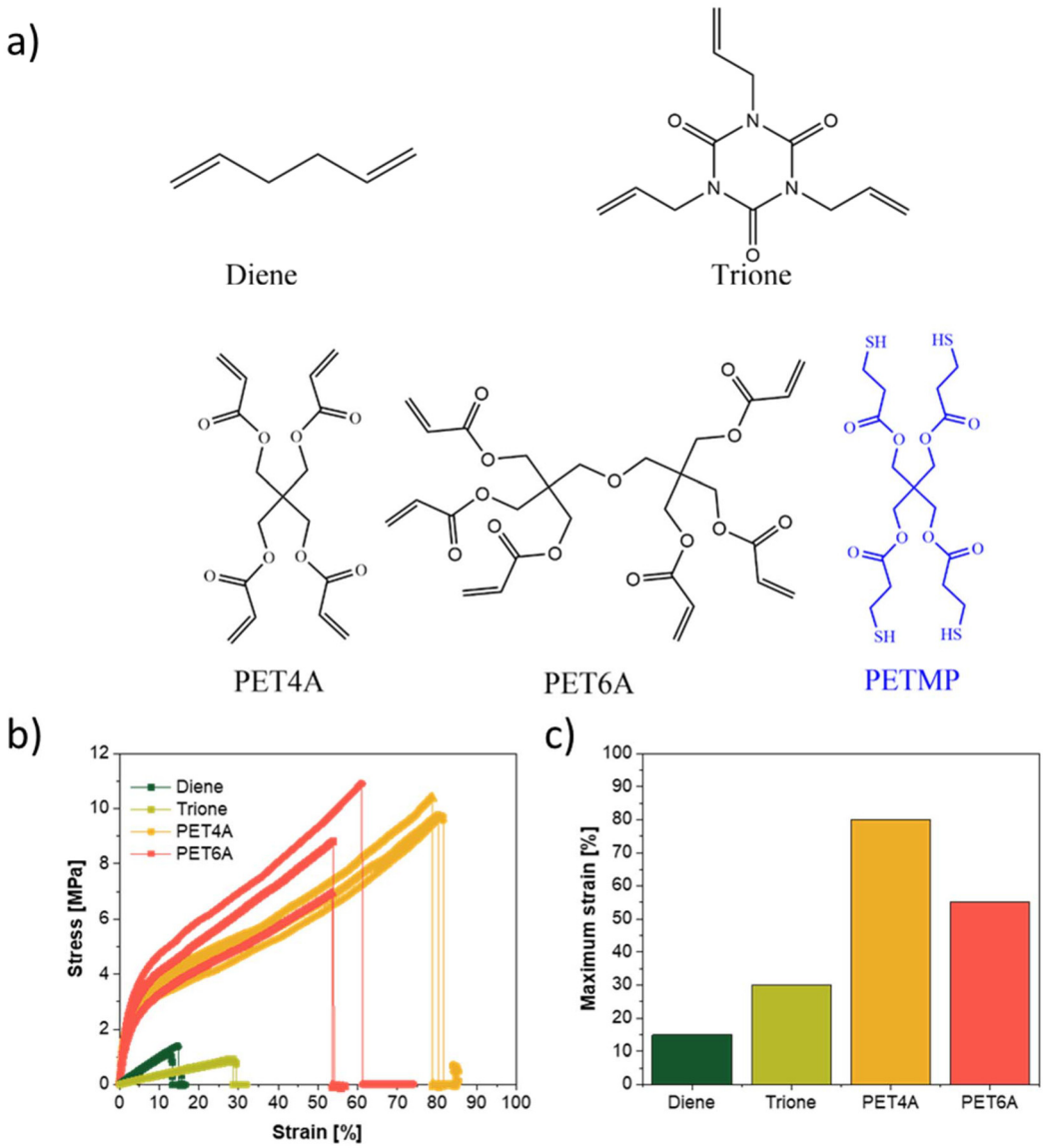

Fig. 4 (a) Structure of the backbone monomers used to synthesize the diene-, trione-, PET4A- and PET6A-SIPEs together with PETMP (in blue). (b) Measured stress–strain curves and (c) the maximum strain of the diene-, trione-, PET4A- and PET6A-SIPEs. The tests, at least duplicated, were performed on neat SIPEs, *i.e.*, without PVDF-HFP and molecular transporter at RT.

their structures in Fig. 4a). The main difference among the backbone monomers was the number of functional vinyl groups available per molecule. Diene, trione, PET4A, and PET6A have 2, 3, 4, and 6 functional groups, respectively. A higher amount of vinyl groups is expected to create more cross-linking bridges in the resulting SIPE, meaning diene-SIPE was expected to have the lowest degree of cross-linking and PET6A-SIPE the highest. This would enable us to fabricate SIPEs with various networks, offering different mechanical and electrochemical properties. For example, it is expected that the PET6A will provide higher mechanical properties due to its high cross-link degree. However, the formated cavities might be small enough to hinder Na^+ transport. Therefore, a deep characterization is conducted and shown below to understand the influence of the backbone components on the SIPE properties.

The mechanical properties of the different cross-linked SIPEs were investigated using dry and PVDF-HFP-free SIPEs for a direct comparison. The SIPEs were exposed to strain while measuring the stress until failure (Fig. 4b). Additionally, the maximum elongation that the SIPEs can withstand before breaking is illustrated in Fig. 4c. The diene- and trione-SIPE were rigid, not showing any linear elastic region that follows Hooke's law of elastic deformation in the stress–strain curves, indicating that an increased force did not proportionally extend the polymer. Instead, these two SIPEs directly entered the strain hardening region upon elongation, exhibiting the lowest elongation values, 15% for diene- and 30% for trione-SIPE. The diene-SIPE, which contains only two functional groups (*i.e.*, two cross-link sites), owns the poorest binding strength inside the polymer backbone among all SIPEs. Additionally, the diene molecule was relatively rigid and could not accommodate an increasing amount of stress, resulting in the lowest maximum strain value. Although the trione-SIPE had an additional functional group providing enhanced mechanical stability, the molecule itself is also not-flexible, which explain the observed behavior.

On the other hand, both PET4A- and PET6A-SIPEs exhibited linear elastic deformation at the beginning of the stress–strain curves and high strain resistance, exceeding 50%, as both molecules are more flexible and contain more functional groups, allowing for the production of a densely crosslinked SIPE structure. Noteworthy, PET6A-SIPE exhibited 55% maximum strain, while PET4A-SIPE reached 80%. The chemical structure can explain the better mechanical properties of PET4A-SIPE. PET6A features an ether bond in the middle of its structure, connecting the two sides of the molecule (see Fig. 4a). This ether bond breaks, generating an oxygen radical and a tertiary carbon radical, which are both stable intermediate states.[29] Thus, the PET6A molecule could break more easily compared to the "core" of PET4A, which is based on four C–C bonds. In summary, the PET4A-SIPE exhibited the highest strain resistance, as PET4A provided the most flexible backbone monomer among the tested SIPEs and had a stable "core" in the middle of its structure.

The thermal stability of the dry diene-, trione-, PET4A-, and PET6A-based SIPEs blended with PVDF-HFP was investigated by TGA up to 600 °C (Fig. 5a). All SIPEs exhibited thermal stability up to 270 °C, *i.e.*, less than 5% weight loss, indicating that the backbone component had no significant influence on the thermal properties. The diene-SIPE showed a slightly sharper mass loss right after passing the decomposition temperature, *i.e.*, a higher decomposition rate, due to the lowest amount of cross-linking bonds in the backbone structure. In addition, DSC measurements were performed from −20 °C up to 200 °C and back to −20 °C. The DSC scans (Fig. 5b) showed a T_g peak between 30 and 50 °C and a T_c around 100 °C for all SIPEs, without significant differences among them.

The SWAXS patterns of the PVDF-HFP-free and PVDF-HFP-blended SIPEs composed of either diene-, trione-, PET4A- or PET6A-based backbones were recorded (see Fig. 6). Additionally, the SWAXS patterns of a neat PVDF-HFP membrane and a commercially available PVDF membrane were measured as references. The WAXS pattern of the PVDF

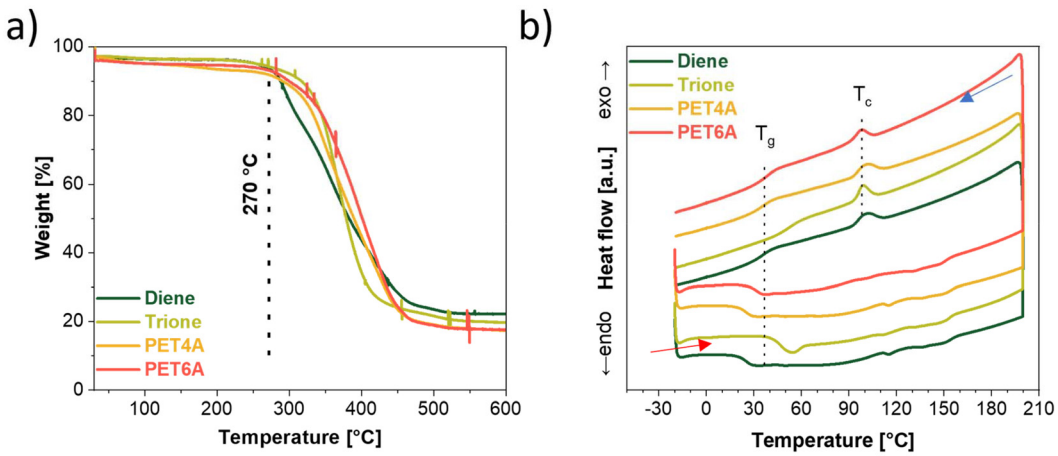

Fig. 5 (a) TGA and (b) DSC of dry diene-, trione-, PET4A- and PET6A-based SIPEs (heating rate of 5 °C min^{-1}, inert N_2 atmosphere, the DSC was performed by two cooling and heating cycles between −20 and 200 °C).

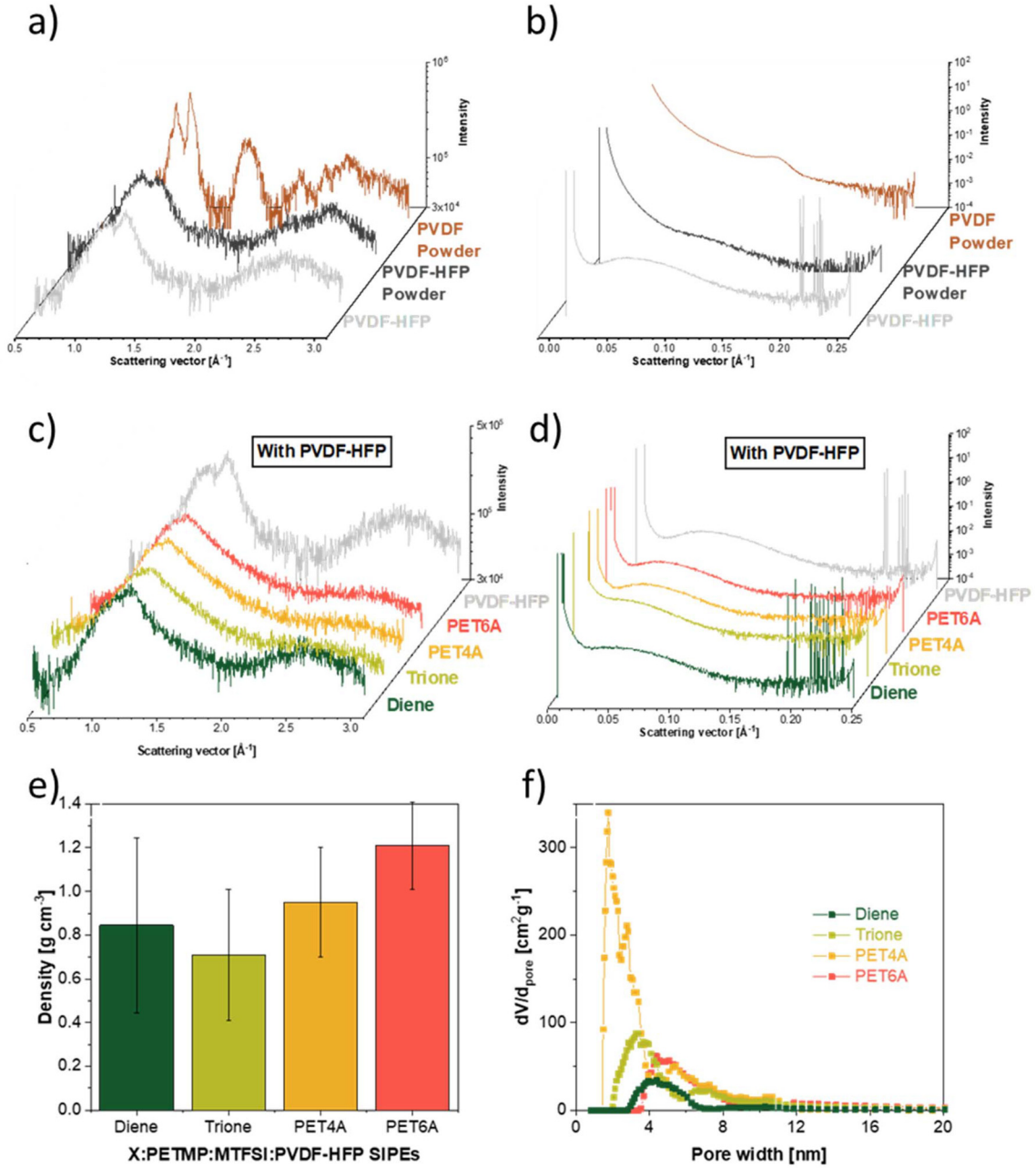

Fig. 6 (a) WAXS and (b) SAXS patterns of commercial PVDF and PVDF-HFP powders, and PVDF-HFP membrane. (c) WAXS and (d) SAXS patterns, (e) density and (f) calculated pore size of the dry diene-, trione-, PET4A- and PET6A-SIPEs blended with PVDF-HFP.

powder (Fig. 6a) displayed the typical Bragg peaks of crystalline PVDF at q values of 1.15 $Å^{-1}$, 1.28 $Å^{-1}$, 1.81 $Å^{-1}$ and 2.66 $Å^{-1}$,[30,31] indicating a semicrystalline structure. Meanwhile, the PVDF-HFP copolymerization led to a significant amorphization for both the powder and the membrane, as suggested by the peak intensity decrease and broadening, coupled with the appearance of a broad halo and a complete intensity loss at 1.81 $Å^{-1}$.[32]

Further information about the structure was obtained by comparing the SAXS patterns (Fig. 6b). The PVDF powder showed a slightly visible peak at 0.135 $Å^{-1}$, while no clear peak was seen for the PVDF-HFP powder, which is in good agreement with the more amorphous structure of the latter, as observed *via* WAXS. The change in intensity and q values from PVDF to PVDF-HFP suggests that the copolymerization with HFP results in a decrease of crystallinity and an increase of the average distance between the lamellar domains. However, once PVDF-HFP is cast into a membrane, a broad peak emerges at 0.07 $Å^{-1}$, indicating that the casting process facilitates a more pronounced orientation.

SIPEs composed of the four polymer backbones (*i.e.*, diene-, trione, PET4A or PET6A) were analyzed without (Fig. S7) and

with (Fig. 6c and d) PVDF-HFP. All investigated PVDF-HFP-free SIPE membranes exhibited a broad peak between 0.5 and 1.5 $Å^{-1}$ in the WAXS pattern, a characteristic typically observed in amorphous polymers. In fact, the SAXS patterns are in agreement with the WAXS pattern, displaying no sharp peaks, which suggests a random orientation of the polymer over long distances and confirms the rather amorphous polymer structure.

The WAXS patterns of SIPEs blended with 20% PVDF-HFP (Fig. 6c) exhibited similarities with those of PVDF-HFP-free, such as a broad peak between 0.5 and 1.5 $Å^{-1}$, which is characteristic of amorphous structures. In fact, the peak at 2.7 $Å^{-1}$ displayed by PVDF-HFP was not observed for the SIPE membranes, except for the diene-SIPE, suggesting either larger pores or higher flexibility of the membranes.[30] Regarding the SAXS patterns, all SIPE (Fig. 6d) and neat PVDF-HFP membranes showed a broad peak at around 0.06–0.08 $Å^{-1}$, which is characteristic of the long-distance repeating unit of PVDF-HFP. However, the broad peak that pure PVDF-HFP shows at 0.08 $Å^{-1}$ was shifted towards 0.06 $Å^{-1}$ for SIPEs. The peak shift towards smaller q values suggests that the distance between the vinylidene fluoride units increased once included in the polymer network, not forming subclusters, but rather being homogeneously incorporated into the SIPE network.

Additional insights into the SIPE structure were obtained from density measurements (Fig. 6e), which ranged from 0.7 to 1.2 g cm^{-3}. The density increased with the addition of functional groups, except for diene-SIPE, which exhibited a higher density than trione-SIPE despite having fewer crosslinks. This suggests that the least crosslinked structure formed a denser polymer backbone structure, presumably due to the reduced size of the flexible diene molecule.

BET assessed the intrinsic porosity and the pore size distribution. The Ar isotherms were measured for all SIPEs (Fig. S8), and the pore size distribution was analyzed (Fig. 6f), revealing pore sizes ranging from 2 to 8 nm. The diene-SIPE exhibited a pore size distribution ranging from 3 to 6 nm. The trione-SIPE, on the other hand, exhibited two distinct pore sizes: one ranging from 3 to 5 nm and another from 6 to 8 nm. The PET4A displayed the smallest pore size (between 1 and 4 nm) with a lower content of pores in the 5–8 nm range. Lastly, the PET6A-SIPE exhibited a pore size ranging from 4 to 8 nm. In summary, the trione-SIPE with the lowest density exhibited the largest pores, confirming its high porosity, which is likely due to its rigid structure. The PET4A- and trione-based SIPEs also featured pores with a size below 4 nm. This second type of pores could originate from interlocking chains between the same molecule, forming a closed ring rather than a network with multiple bonding partners and thus creating a second type of cavity with a different pore width. The absence of this second peak for the diene- and PET6A-SIPEs can be explained by the fact that the diene molecule is hindered from forming closed rings due to the low number and wide spacing of its functional groups. The PET6A molecule has enough functional groups to create these ring closings. The BET results align with the density and SWAXS measurements, confirming the differences in the porous structures of the various backbones.

The SIPEs were soaked with the EC:DMC:FEC (49:49:2 vol. %) molecular transporter, and their ionic conductivity was measured (Fig. 7a). As expected, the SIPEs' conductivity increased with temperature and exhibited the VTF behavior (see Fig. S9 for comparison with $\ln(\sigma)$ *vs.* $1000/T$ plot), typical of polymeric ion conductors. Comparing the ionic conductivity among the four SIPEs, the diene- and trione-SIPEs displayed slightly higher values at all measured temperatures (around $\times 10^{-4}$ S cm^{-1} at 20 °C and 6.0×10^{-4} S cm^{-1} at 90 °C) compared to PET4A- and PET6A-SIPEs (around $\times 10^{-5}$ S cm^{-1} at 20 °C and 4.0×10^{-4} S cm^{-1} at 90 °C). The ionic conductivity results indicated that a lower amount of cross-linking and lower density promote faster ion transport throughout the membrane.

The electrochemical stability window of the SIPEs was measured using Al|SIPE|Na cells (Fig. 7b). The cathodic stabi-

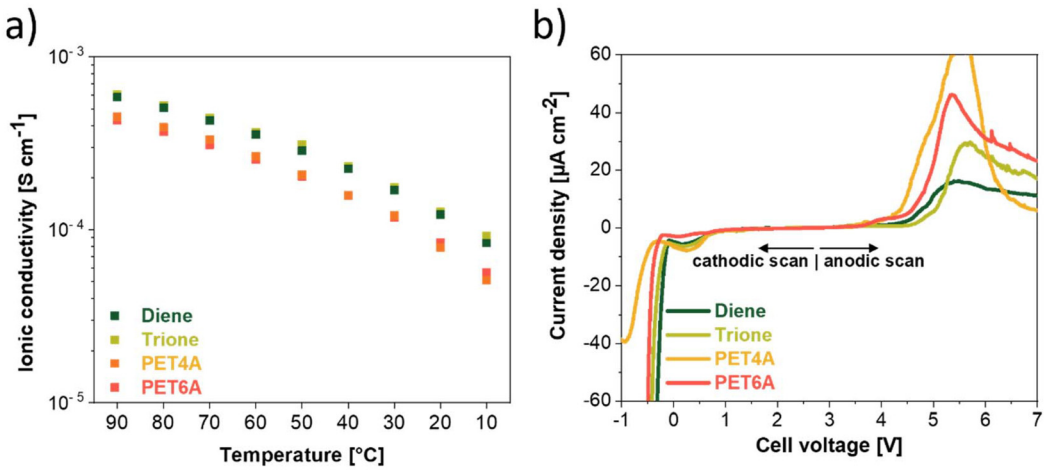

Fig. 7 (a) Temperature-dependent ionic conductivity, and (b) electrochemical stability window (Al||SIPE||Na; scan rate: 30 µV s^{-1}; temperature: 40 °C) of the diene-, trione-, PET4A- and PET6A-SIPE containing 50 wt.% of molecular transporters (EC:DMC:FEC).

lity showed no electrochemical limitation prior to Na metal plating, except for a very small reduction peak at 0.4 V, attributed to the decomposition of EC, DMC, and/or FEC. Meanwhile, the anodic scan showed excellent stability (above 4 V, considering the threshold for the voltage onset >25 μA cm^{-2}) for all SIPEs.

The SIPEs were then used as electrolytes in quasi-solid-state Na|SIPE|PW cells. The cell voltage profiles (Fig. 8a–d) exhibited characteristic plateaus at approximately 3.0 and 3.3 V vs. Na^+/Na, regardless of the backbone structure. The initial charge and discharge capacities of the cells were 188 and 184 mAh g^{-1} for the diene-SIPE-based cell, 186 and 176 mAh g^{-1} for the trione-SIPE, 155 and 143 mAh g^{-1} for the PET4A-SIPE, and 167 and 159 mAh g^{-1} for the PET6A-SIPE. The initial charge capacity of all cells was higher than the theoretical capacity of PW, suggesting that some side reactions affecting the electrolyte occur at the PW and/or Na electrodes. The diene- and trione-SIPE exhibited a higher initial specific capacity due to the higher ionic mobility, which reduced the cell polarization. This resulted in a longer first plateau of 86 and 82 mAh g^{-1} for the diene- and trione-based SIPEs, respectively, while the PET4A- and PET6A-based SIPEs cells delivered 65 and 67 mAh g^{-1}, respectively. The initial Coulombic efficiency was comparable for all SIPEs, *e.g.*, 97%, 94%, 92%,

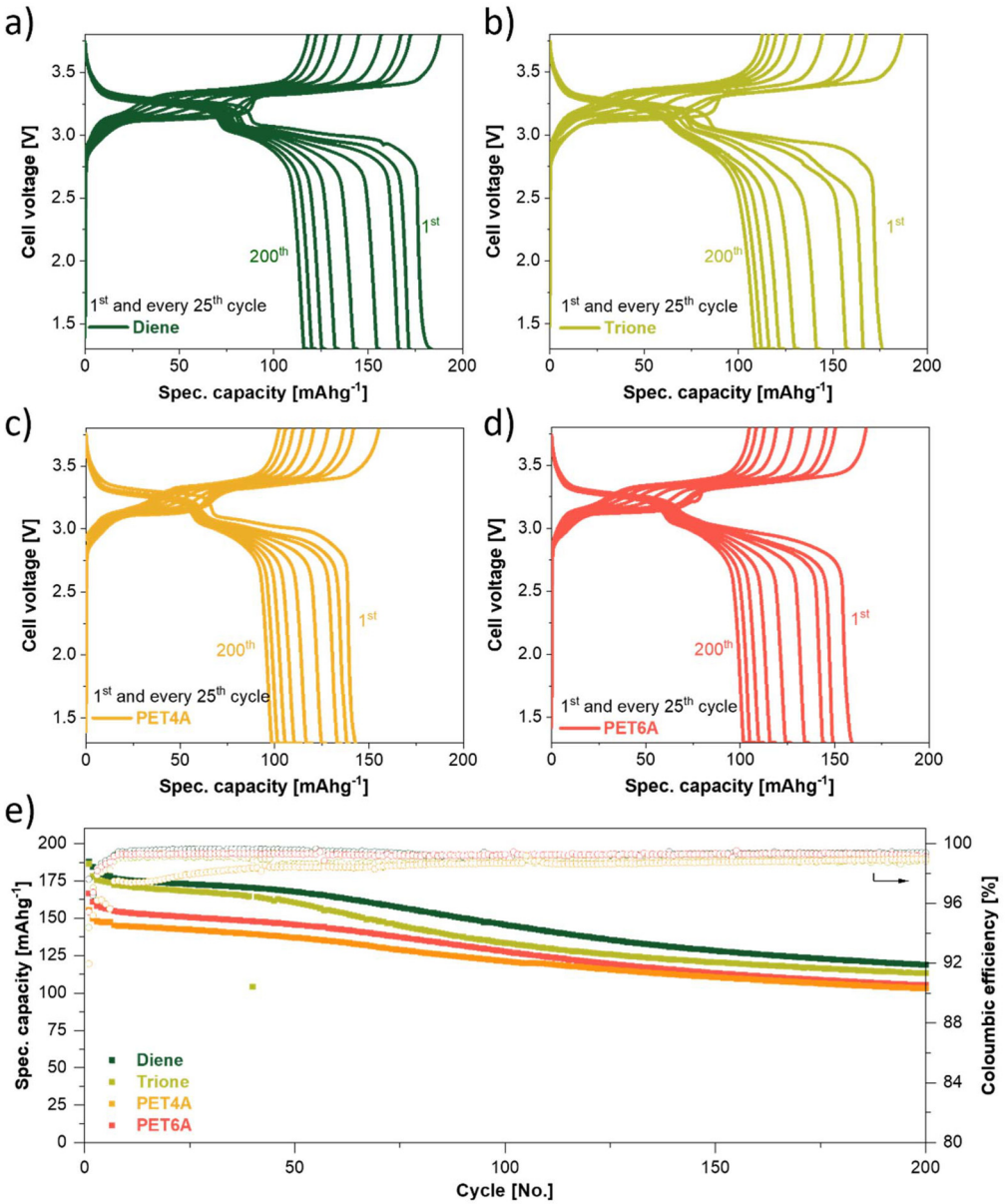

Fig. 8 Voltage profile of Na||SIPE||PW cells, containing (a) diene-, (b) trione-, (c) PET4A- and (d) PET6A-SIPE and the corresponding (e) cycling performance (capacity *vs.* cycle number and the corresponding coulombic efficiency). Galvanostatic cycling tests are performed at C/50 (1st cycle), followed by C/20 (5 cycles) and C/10 until failure between 3.8 V and 1.3 V. All measurements were performed at 40 °C. The SIPEs contain 50 wt.% of EC:DMC:FEC.

and 95% for diene-, trione-, PET4A, and PET6A, respectively, suggesting that the choice of backbone monomer slightly influenced SEI and CEI formation.

Furthermore, the discharge capacity and Coulombic efficiency upon prolonged cycling are illustrated in Fig. 8e. The capacity after 200 cycles was 119 mAh g^{-1} for the diene-SIPE, 113 mAh g^{-1} for the trione-SIPE, 103 mAh g^{-1} for the PET4A-SIPE, and 105 mAh g^{-1} for the PET6A-SIPE-based cells, with corresponding capacity retention rates of 68%, 66%, 73%, and 68%, respectively. The low Coulombic efficiency of the PET4A-SIPE upon cycling suggests that the close-knit network of the PET4A-SIPE results in a stiff membrane, thereby reducing contact with the electrodes compared to other SIPEs, which may lead to limited discharge and lower Coulombic efficiency. The diene-based SIPE offered slightly better ion transport compared to all other tested SIPEs. Still, it also exhibited the weakest mechanical stability, which may be related to its more pronounced capacity fading. Meanwhile, the PET4A- and PET6A-SIPE offer higher mechanical stability, but slightly lower ionic conductivity and cycling performance.

Conclusion

The influence of the side-chain spacer on NaSTFSI, NaMTFSI and NaFTFSI SSM was investigated. The results revealed that the flexible and fluorinated NaFTFSI SSM, although it exhibited the highest ionic conductivity, largely suffered from an extended decomposition reaction with Na metal, leading to poor cycling stability. On the contrary, the NaMTFSI-based one was, overall, the best performing SIPE, showing an ionic conductivity of 7.9×10^{-5} S cm^{-1} at 20 °C (4.5×10^{-4} S cm^{-1} at 90 °C) and the PW cell containing such SIPE delivered a specific capacity of 103 mAh g^{-1} after 200 cycles at 0.1 C. In addition, the influence of the backbone components on the electrochemical properties of NaMTFSI, PETMP and PVDF-HFP SIPE, together with either diene, trione, PET4A or PET6A, was also investigated. The number of cross-linking sites increased from diene (2) to PET6A (6), indicating that a lower number of cross-linking resulted in larger pores and higher ionic conductivity, but reduced mechanical stability. The diene-SIPE showed the highest ionic conductivity of 1.8×10^{-4} S cm^{-1} at 20 °C and 6.0×10^{-4} S cm^{-1} at 90 °C. The manufactured cell using Na metal, diene-SIPE and PW delivered a specific capacity of 119 mAh g^{-1} after 200 cycles at 0.1 C. Although the results were promising, they revealed the need to investigate the chemistry of the SIPE components further to enhance their physicochemical, mechanical, and electrochemical properties – with the ultimate goal of manufacturing high-performance quasi-solid-state Na-metal batteries.

Author contributions

C. W.: investigation, methodology, data analysis, visualization, writing—original draft & editing. L. H.: SWAXS analysis. L. G.: synthesis of the NaFTFSI monomer. A. V.: supervision, review, and editing. D. B.: supervision, review, and editing. M. Z.: conceptualization, methodology, investigation, formal analysis, project administration, supervision, writing – review and editing. S. P.: conceptualization, methodology, investigation, formal analysis, funding acquisition, project administration, supervision, writing—review and editing.

Conflicts of interest

There are no conflicts to declare.

Data availability

The data that support the findings of this study are available from the corresponding author upon reasonable request. The data supporting this article have been included as part of the supplementary information (SI). Supplementary information is available. See DOI: https://doi.org/10.1039/d5eb00145e.

Acknowledgements

This work was funded by the HORIZON 2020 program (Project "SIMBA", Grant Agreement No. 963542). The authors thank the Helmholtz Association for the financial support. The von Delius group at Ulm University is acknowledged for the solution NMR measurements, Dr C. Klein for the mechanical property's measurements, and Altris AB for providing the Prussian White cathode material.

References

1 M. Li, J. Lu, Z. Chen and K. Amine, *Adv. Mater.*, 2018, **30**, 1800561.
2 H. Bajolle, M. Lagadic and N. Louvet, *Energy Res. Soc. Sci.*, 2022, **93**, 102850.
3 Y. Wang, S. Song, C. Xu, N. Hu, J. Molenda and L. Lu, *Nano Mater. Sci.*, 2019, **1**, 91–100.
4 L. Qiao, X. Judez, T. Rojo, M. Armand and H. Zhang, *J. Electrochem. Soc.*, 2020, **167**, 070534.
5 https://www.woodmac.com/news/opinion/sodium-ion-batteries-disrupt/(2025).
6 C. Zhao, L. Liu, X. Qi, Y. Lu, F. Wu, J. Zhao, Y. Yu, Y.-S. Hu and L. Chen, *Adv. Energy Mater.*, 2018, **8**, 1703012.
7 K. Chayambuka, G. Mulder, D. L. Danilov and P. H. L. Notten, *Adv. Energy Mater.*, 2018, **8**, 1800079.
8 I. Hasa, S. Mariyappan, D. Saurel, P. Adelhelm, A. Y. Koposov, C. Masquelier, L. Croguennec and M. Casas-Cabanas, *J. Power Sources*, 2021, **482**, 228872.
9 P. K. Nayak, L. Yang, W. Brehm and P. Adelhelm, *Angew. Chem., Int. Ed.*, 2018, **57**, 102–120.
10 J. Xie and Y. Lu, *Adv. Mater.*, 2025, **37**, 2312451.

11 Q. Liu, Z. Geng, C. Han, Y. Fu, S. Li, Y.-b. He, F. Kang and B. Li, *J. Power Sources*, 2018, **389**, 120–134.
12 G. Xi, M. Xiao, S. Wang, D. Han, Y. Li and Y. Meng, *Adv. Funct. Mater.*, 2021, **31**, 2007598.
13 J. W. Fergus, *J. Power Sources*, 2021, **195**, 4554–4569.
14 J. Chai, Z. Liu, J. Ma, J. Wang, X. Liu, H. Liu, J. Zhang, G. Cui and L. Chen, *Adv. Sci.*, 2017, **4**, 1600377.
15 J. Mindemark, M. J. Lacey, T. Bowden and D. Brandell, *Prog. Polym. Sci.*, 2018, **81**, 114–143.
16 D. Kumar and S. A. Hashmi, *J. Power Sources*, 2010, **195**, 5101–5108.
17 R. Peklar, U. Mikac and I. Serša, *Batteries*, 2024, **10**, 165.
18 J. L. Olmedo-Martínez, A. Fdz De Anastro, M. Martínez-Ibañez, A. J. Müller and D. Mecerreyes, *Energy Fuels*, 2023, **37**, 5519–5529.
19 X. Dong, X. Liu, H. Li, S. Passerini and D. Bresser, *Angew. Chem., Int. Ed.*, 2023, **62**, e202308699.
20 C. Wunder, T.-L. Lai, E. Sic, E. De Vito, G. Buntkowsky, M. Zarrabeitia and S. Passerini, *J. Mater. Chem. A*, 2024, **12**, 20935–20946.
21 G. Rollo-Walker, N. Malic, X. Wang, J. Chiefari and M. Forsyth, *Polymers*, 2021, **13**, 4127.
22 J. Li, H. Zhu, X. Wang, M. Armand, D. R. MacFarlane and M. Forsyth, *Electrochim. Acta*, 2015, **175**, 232–239.
23 H.-D. Nguyen, G.-T. Kim, J. Shi, E. Paillard, P. Judeinstein, S. Lyonnard, D. Bresser and C. Iojoiu, *Energy Environ. Sci.*, 2018, **11**, 3298–3309.
24 A. Mayer, A. Mariani, X. Dong, G. Vansse, P. Theato, C. Iojoiu, S. Passerini and D. Bresser, *Macromolecules*, 2023, **56**, 2505–2514.
25 M. Worzakowska, K. Sztanke and M. Sztanke, *Int. J. Mol. Sci.*, 2024, **35**, 4768.
26 U. Gradišar Centa, M. Mihelčič, V. Bobnar, M. Remškar and L. Slemenik Perše, *Coatings*, 2022, **12**, 1241.
27 H. Guan, Z. Guo, J. Ding and F. Lian, *J. Appl. Polym. Sci.*, 2016, **133**, 43510.
28 S. Das and A. Ghosh, *Electrochim. Acta*, 2015, **171**, 59–65.
29 H. Zipse, *Radicals in Synthesis I*, ed. A. Gansäuer, Springer Berlin Heidelberg, Berlin, Heidelberg, 2006, vol. 263, pp. 163–189.
30 T. A. Ezquerra, A. Nogales, M. C. García-Gutíerrez, E. Rebollar, O. Galvez, I. Sics and M. Malfois, *Polymer*, 2022, **249**, 124827.
31 M. Li, H. J. Wondergem, M.-J. Spijkman, K. Asadi, I. Katsouras, P. W. M. Blom and D. M. de Leeuw, *Nat. Mater.*, 2013, **12**, 433–438.
32 A. Maurya, E. Mias, J. Schoeller, I. E. Collings, R. M. Rossi, A. Dommann and A. Neels, *Nanoscale Adv.*, 2022, **4**, 491–501.